

Non-modal disturbances growth in a viscous mixing layer flow

This content has been downloaded from IOPscience. Please scroll down to see the full text.

2014 Fluid Dyn. Res. 46 041414

(<http://iopscience.iop.org/1873-7005/46/4/041414>)

View [the table of contents for this issue](#), or go to the [journal homepage](#) for more

Download details:

IP Address: 132.66.194.11

This content was downloaded on 27/05/2014 at 07:28

Please note that [terms and conditions apply](#).

Non-modal disturbances growth in a viscous mixing layer flow

H Vitoshkin and A Yu Gelfgat

School of Mechanical Engineering, Faculty of Engineering, Tel-Aviv University,
Ramat Aviv, 69978 Tel-Aviv, Israel

E-mail: gelfgat@tau.ac.il

Received 6 October 2013

Accepted for publication 4 March 2014

Published 22 April 2014

Communicated by M Asai and A Oron

Abstract

The non-modal transient growth of disturbances in an isothermal viscous mixing layer flow is studied for Reynolds numbers varying from 100 up to 5000 at different streamwise and spanwise wavenumbers. It is found that the largest non-modal growth takes place at the wavenumbers for which the mixing layer flow is stable. In linearly unstable configurations, the non-modal growth can only slightly exceed the exponential growth at short times. Contrarily to the fastest exponential growth, which is two-dimensional, the most profound non-modal growth is attained by oblique three-dimensional waves propagating at an angle with respect to the base flow. By comparing the results of several mathematical approaches, it is concluded that within the considered mixing layer model with a *tanh* base velocity profile, the non-modal optimal disturbances growth is governed only by eigenvectors that are decaying far from the mixing zone. Finally, a full three-dimensional DNS with optimally perturbed base flow confirms the presence of the structures determined by the transient growth analysis. The time evolution of optimal perturbations is presented. It exhibits a growth and a decay of flow structures that sometimes become similar to those observed at the late stages of the time evolution of the Kelvin–Helmholtz billows. It is shown that non-modal optimal disturbances yield a strong mixing without a transition to turbulence.

(Some figures may appear in colour only in the online journal)

1. Introduction

In parallel shear flows, there can be a transient amplification (or growth) of a disturbance energy even when all of the eigenvalues of the linearized problem indicate perturbation decay.

This phenomenon, which occurs at relatively short times, is widely recognized as ‘transient’ or ‘non-modal’ growth. The growth is caused by a non-orthogonality of the flow eigenmodes, and the result is independent of whether or not the shear flow is linearly unstable due to exponentially growing disturbances (see, e.g., Ellingsen and Palm 1975, Landahl 1980).

The non-modal growth of disturbances is well studied for bounded shear flows, e.g., for plane Couette and Poiseuille flows (Farrel 1987, 1988; Buttler and Farrell 1992; Reddy and Henningson 1993; Schmid and Henningson 2001). The semi-unbounded Blasius boundary layer flow has been extensively investigated as well (see, e.g., Andersson *et al* 1999, Schmid 2000, Åkervik *et al* 2008, Corbett and Bottaro 2000). However, the problem of non-modal growth in fully unbounded flows, such as a mixing layer and a jet flow, is not completely understood. In this paper, we consider the problem of the transient non-modal growth of disturbances in a mixing layer flow with a hyperbolic tangent velocity profile. This flow is unstable within the inviscid model, and becomes linearly unstable at a low Reynolds number, if the viscous flow model is implied. The flow remains linearly stable for a streamwise wavenumber larger than unity (Drazin and Reid 2001, Gaster *et al* 1985). However, the instability development at early times still can be subjected to a non-modal growth, so the issue should be studied for the mixing layer flow as well.

The initial growth in the inviscid mixing layer flow was studied by Bun and Criminale (1994) and Criminale and Jackson (1995). They showed that a temporal perturbation growth in a mixing layer is possible. Later Le Dizès (2003) examined the non-modal growth of two-dimensional disturbances in inviscid and viscous mixing layer flows. It is shown in the present paper that the growth of three-dimensional perturbations is expected to be larger. Yecko *et al* (2002) and Yecko and Zaleski (2005) studied the non-modal growth in a two-phase mixing layer for three-dimensional disturbances. They found that the largest non-modal growth results from two-dimensional perturbations located in the spanwise plane and is uniform in the streamwise direction. Recently, Arratia *et al* (2013) reported three-dimensional non-modal growth in a viscous mixing layer with the *tanh* velocity profile at $Re = 1000$. Those authors focused mainly on short times and wavenumbers relating to linearly unstable regimes. In the present study we show that at short times a large non-modal growth can be attained by optimal perturbations whose wavenumbers correspond to linearly stable configurations.

Heifetz and Methven (2005) interpreted the optimal perturbation growth in an inviscid mixing layer in terms of the counter propagating Rossby waves. Bakas and Ioannou (2009) studied the non-modal growth of two-dimensional disturbances in an inviscid mixing layer with a free surface. Those papers focused on the early transient disturbances evolution in the mixing layer flow. Surprisingly, the non-modal three-dimensional growth of a single-phase viscous mixing had not been addressed until the above-cited study Arratia *et al* (2013) and some preliminary results of Vitoshkin *et al* (2012). A rather strong initial growth was observed in experiments¹ of Gaster *et al* (1985) and Kit *et al* (2007), in which the initial disturbance was excited externally with prescribed streamwise (Gaster *et al* 1985), and streamwise and spanwise (Kit *et al* 2007), wavelengths. These experiments motivated the presented work. In the course of this study, we did not discover any surprisingly large non-modal transient growth that can be observed in the mixing layer flow. However, we believe that the results reported below complement the common understanding of the mixing layer flow’s properties and its behavior at early times. In addition to that, we show that if perturbation streamwise and spanwise wavelengths can be externally controlled as in, e.g., Gaster *et al* (1985), Gelfgat and Kit (2006) and Kit *et al* (2007), the non-modal growth can be used as a means of effective mixing, keeping the flow fully laminar.

¹ Private communication with E Kit.

In this work, a transient non-modal growth of disturbances in a mixing layer flow is studied numerically. This flow is known to be linearly unstable either if the inviscid flow is considered, or starting from rather low Reynolds numbers when the viscous flow model is implemented. The numerical code, based on the finite difference discretization of the Orr–Sommerfeld and Squire equations, is verified against well-known results on plane Poiseuille and Blasius boundary flows. The results for non-modal disturbances growth in the mixing layer flow are obtained for a Reynolds number varied from 100 to 5000. It is shown that, as expected and explained by Vitoshkin (2013), at short times the largest growth is attained by three-dimensional disturbances whose wavenumbers lie beyond the interval where the flow is linearly unstable.

Finally, we generated the initial data for three-dimensional direct numerical simulations using calculated three-dimensional optimal perturbations. Fully non-linear 3D computations allow us to confirm the previous findings, as well as to explore the non-linear evolution of optimal disturbances into the viscous mixing layer flow. We show that an initially small-amplitude optimal disturbance can grow so that non-linear terms become significant, which leads to the formation of flow structures qualitatively different from the well-known Kelvin–Helmholtz (KH) billows at early stages of the instability onset. The optimal disturbances grow and decay in time, yielding, in particular, a significant mixing inside the shear zone. It is quite an exceptional case of mixing since it is not followed by any transition to turbulence, which may be practically important.

Comparing the above flow structures with the experimental and numerical results on the developing mixing layer flows, we have found that similar flow patterns are observed at late stages of the non-linear development of the KH instability. We argue that at long times after the onset of linear instability, the effective width of the mixing layer grows so that the wavelength scaled by the width diminishes, while the corresponding wavenumber grows. As a result, the stable mixing layer configuration is created. This configuration is necessarily perturbed by the time-developing flow, which can trigger non-modal growth resulting in similar flow structures.

In the following, we give a brief formulation of the problem (section 2) and describe the solution techniques applied and the test calculations made (section 3). In section 4 we discuss the effect of discrete and continuous spectra on the non-modal growth in the considered flow. The main results are presented in section 5. We start from the growth functions and the optimal perturbation patterns yielded by the non-modal analysis. Then we study the time evolution of the optimal disturbances within linear and non-linear and two- and three-dimensional models. Our conclusions are summarized in section 6.

2. Problem formulation

We consider an isothermal incompressible mixing layer flow produced by two fluid layers moving with opposite velocities $\pm U_{max}$ in the x -direction. Assuming that the mixing layer characteristic width is δ_v , the hyperbolic tangent velocity profile $U(z) = U_{max} \tanh(z/\delta_v)$ is taken as a base flow. We are interested in the temporal evolution of a small three-dimensional disturbance $\mathbf{v} = (u, v, w)^T$, which is governed by the non-dimensional momentum and continuity equations

$$\begin{aligned} \left(\frac{\partial}{\partial t} + U \frac{\partial}{\partial x} \right) \mathbf{v} + \frac{dU}{dz} w \mathbf{e}_x + (\mathbf{v} \cdot \nabla) \mathbf{v} &= -\nabla p + \frac{1}{Re} \Delta \mathbf{v}, \\ \nabla \cdot \mathbf{v} &= 0. \end{aligned} \quad (1)$$

were $\mathbf{v} = (u, v, w)$ is the velocity with components in the streamwise (x), spanwise (y) and vertical (z) directions; p is the pressure and Δ denotes the vector Laplacian operator. The

equations are rendered dimensionless using the scales δ_v , U_{max} , δ_v/U_{max} and ρU_{max}^2 for length, velocity, time and pressure, respectively. The Reynolds number is defined by $Re = U_{max} \delta_v / \nu$, where ν is the kinematic viscosity.

The flow is assumed to be periodic in the spanwise and streamwise directions, so that we consider the normal mode expansion and study solutions with fixed wavenumbers α and β in the x - and y -directions. Since the temporal stability problem is considered, both wavenumbers are real. Looking for the infinitesimal perturbations of the base flow in the form $\{u(z,t), v(z,t), w(z,t), p(z,t)\} \exp(i\alpha x + i\beta y)$ and using the standard derivation procedure, we arrive at the set of Orr–Sommerfeld (OS) and Squire equations:

$$\Delta \frac{\partial w}{\partial t} = i\alpha \left(\frac{d^2 U}{dz^2} w - U \Delta w \right) + \frac{1}{Re} \Delta^2 w, \quad (2)$$

$$\frac{\partial \eta}{\partial t} = -i\beta \frac{dU}{dz} w + \left(\frac{1}{Re} \Delta - i\alpha U \right) \eta \quad (3)$$

in which w and η are the vertical component of the velocity, w , and the vertical component of the vorticity, respectively (see e.g., Schmid and Henningson 2001). Here, the Laplacian operator reduces to $\Delta = \partial^2 / \partial z^2 - (\alpha^2 + \beta^2)$. The problem is considered for $t > 0$ and $-L \leq z \leq L$, where L must be large enough to ensure results independence on further increase of L . In order to make our analysis compatible with the previous numerical studies (e.g., Kit *et al* 2010, Rogers and Moser 1992), we assume that all the perturbations vanish at $z = \pm L$.

In the following, we study the initial temporal growth of a perturbation in terms of the kinetic energy norm, produced by the corresponding inner product (the star denotes the complex conjugate):

$$E(t) = \langle \mathbf{v}, \mathbf{v} \rangle = \int_V \mathbf{v}^* \cdot \mathbf{v} dV, \quad \text{where } \langle \mathbf{u}, \mathbf{v} \rangle = \int_V \mathbf{u}^* \cdot \mathbf{v} dV \quad (4)$$

We define the optimal disturbance as one yielding the maximum possible amplification of its initial energy norm. Following Farrell (1987, 1988) and Butler and Farrell (1992), the maximal amplification is defined as the maximal possible growth of the perturbation norm at a given time t , and is considered for a single particular set of stability parameters (α, β, Re) . The energy amplification, or growth function $G(t)$, is defined as:

$$G(t) = \max_{E(0) \neq 0} \frac{E(t)}{E(0)}. \quad (5)$$

Clearly, the above formulation remains meaningful only at relatively small times before the viscosity effects widen the flow profile. To estimate these meaningful times for different Reynolds numbers, a simple model of a time-dependent viscous dissipation was considered in Vitoshkin (2013). It was concluded that for $Re \leq 10$, the layer thickness strongly depends on the Reynolds number. For $10 \leq Re \leq 100$, the linearized problem is meaningful only at very short times, $t < 2$; however, it already allows the consideration of the linear stability of the flow. For $Re > 100$ the thickness remains almost unchanged until $t = 30$. Note that the maximal values of the growth functions reported below were reached within this time interval.

3. Solution technique and test calculations

Equations (2) and (3) were discretized using the second-order central finite difference schemes. After discretization, the governing equations are reduced to a system of linear ODEs

Table 1. Convergence of critical energetic Reynolds numbers Re_{crE} and the growth function G_{max} . Comparison with results of Reddy and Henningson (1993) and Schmid (2000).

Number of grid points, N	Poiseuille flow				Blasius boundary layer	
	Re_{crE} $\alpha=0,$ $\beta=1.9$	Re_{crE} $\alpha=3.2,$ $\beta=3$	G_{max} $\alpha=1,$ $\beta=0,$ $Re=3000$	G_{max} $\alpha=0.5,$ $\beta=2.5,$ $Re=1000$	G_{max} $\alpha=0.1,$ $\beta=0.26,$ $Re=1000$	G_{max} $\alpha=0.2,$ $\beta=0.47,$ $Re=1000$
200	49.94	88.83	21.87	198.23	221.96	394.82
300	49.89	88.64	21.47	198.01	219.89	397.06
400	49.87	88.57	20.95	197.57	213.06	398.11
500	49.85	88.51	20.29	197.55	213.64	398.12
600	49.85	88.51	20.28	197.54	213.65	398.13
700	49.85	88.51	20.28	197.54	213.65	398.13
Reddy and Henningson Schmid	49.7	87.6	20.37	196	≈ 200	≈ 400

governed by a matrix \mathbf{L} assembled from all the discretized equations. The spectrum and the eigenvectors of \mathbf{L} were computed using the QR algorithm. The transient growth is studied by three different numerical approaches: (i) using the factorization of the Gram matrix (Reddy and Henningson 1993, Schmid and Henningson 2001) and singular value decomposition (SVD); (ii) applying the calculus of variations (Butler and Farrell 1992); (iii) by iterative forward/backward integration of the governing/adjoint equations (Corbett and Bottaro 2000). All three methods are implemented to cross-verify the results, as well as to support the conclusions of section 4.

For the code verification, we calculated the critical energetic Reynolds number and growth function for the plane Poiseuille flow and Blasius boundary layer profile (table 1). The results are well compared with the published data (Reddy and Henningson 1993 and Schmid 2000). In both cases, using a 600 nodes grid, we observed convergence up to at least the fourth decimal place, and even slightly improved the previous results.

Calculations for the mixing layer flow appear to be significantly more difficult. We observed, for example, that in spite of the well-known stable numerical properties of the QR decomposition, calculations with the quadruple precision are needed to calculate the spectrum accurately. Note that taking the complex conjugate of the eigenvalue problem together with the transformation $z \rightarrow -z$, one can show that anti-symmetry of the base velocity profile implies the appearance of complex eigenvalues in conjugated pairs (see, e.g., Vitoshkin 2013). The corresponding eigenvectors are not complex conjugated, but are located in the opposite midplanes $z \geq 0$ or $z \leq 0$. Use of the double precision instead of the quadruple one leads to spurious numerical errors, which can be seen, for example, as the appearance of non-conjugated pairs of complex eigenvalues.

The computational grid was divided into two parts. A half of the grid points were located inside the interval $-2 \leq z \leq 2$ and were stretched towards the centerline $z=0$. The stretching function used was $\tanh(sy)/\tanh(s)$. The fastest convergence was observed for $s=3$. Remaining parts of the grid above and below the interval $-2 \leq z \leq 2$ were uniform. This grid arrangement yields a strong stretching near the mixing zone, where the linearly most unstable

Table 2. Results for varying lengths of the computational domain L . $Re = 1000$, and the calculation is with 1000 stretched grid points.

L	1 st mode, $\lambda_i=0, \lambda_{real}$		Growth function, G $(t_{max})/t_{max}$	
	$\alpha=1, \beta=0$	$\alpha=0.7, \beta=1$	$\alpha=1, \beta=0$	$\alpha=0.7, \beta=1$
5	-0.0427	-0.1102	98.15/15.5	782.94/24.7
10	-0.0425	-0.1102	98.41/15.7	784.52/24.7
15	-0.0425	-0.1101	98.41/15.7	784.18/24.9
20	-0.0424	-0.1101	98.41/15.7	784.04/24.9
30	-0.0424	-0.1101	98.41/15.7	784.04/24.9
50	-0.0424	-0.1101	98.41/15.7	784.04/24.9
100	-0.0424	-0.1101	98.41/15.7	784.04/24.9

Table 3. Convergence of the four least stable eigenvalues belonging to the discrete spectrum for $\alpha=0.7, \beta=1$ and $Re=1000$ (*tanh*-stretching divided mesh).

Number of grid points, N	1 st mode	2 nd mode	3 rd mode	4 th mode	Growth function, G/t_{max}		
	$\lambda_r, \lambda_i=0$	λ_r	λ_r, λ_i	λ_r, λ_i			
500	-0.1116	-0.2888	-0.3022	-0.1986	-0.3727	0.3068	786.43/25.0
600	-0.1102	-0.3138	-0.3231	-0.1952	-0.3452	0.3032	785.84/24.9
700	-0.1102	-0.3203	-0.3287	-0.1944	-0.3504	0.3025	786.96/24.9
800	-0.1102	-0.3260	-0.3339	-0.1922	-0.3551	0.3013	785.14/24.9
900	-0.1102	-0.3310	-0.3371	-0.1921	-0.3589	0.3001	784.55/24.9
1000	-0.1102	-0.3385	-0.3448	-0.1905	-0.3657	0.2987	784.04/24.9
1100	-0.1102	-0.3385	-0.3445	-0.1902	-0.3653	0.2986	784.04/24.9
1200	-0.1102	-0.3384	-0.3444	-0.1902	-0.3652	0.2986	784.04/24.9
1300	-0.1102	-0.3384	-0.3443	-0.1901	-0.3652	0.2985	784.04/24.9
1400	-0.1102	-0.3383	-0.3441	-0.1901	-0.3650	0.2985	784.04/24.9
1500	-0.1102	-0.3383	-0.3441	-0.1901	-0.3650	0.2985	784.04/24.9

eigenvectors are located (see, e.g., Gelfgat and Kit 2006). Outside the mixing zone, the discrete spectrum eigenvectors decay, so that there is unnecessary stretching is removed. It is emphasized that only this grid arrangement allowed us to obtain grid-independent results with the use of 1000–2000 grid points. The use of continuously stretched or uniform grids with the same amount of grid nodes exhibited an unacceptable grid-dependence.

The computational domain for the mixing layer flow is defined as an interval of width $2L$. According to results of Healey (2009), an insufficiently large value of L can significantly alter flow stability properties. A series of test calculations for L varying between 5 and 100 was carried out together with the necessary convergence study. Dependence of the leading eigenvalue and growth function value on the size of the computational domain L is presented in table 2. Based on several similar calculations for different values of α and β , we concluded that the flow linear stability properties can be described correctly starting from $L=20$. This width of the computational domain corresponds also to the height of the experimental channel (Kit *et al* (2007)), and has been chosen for further computations.

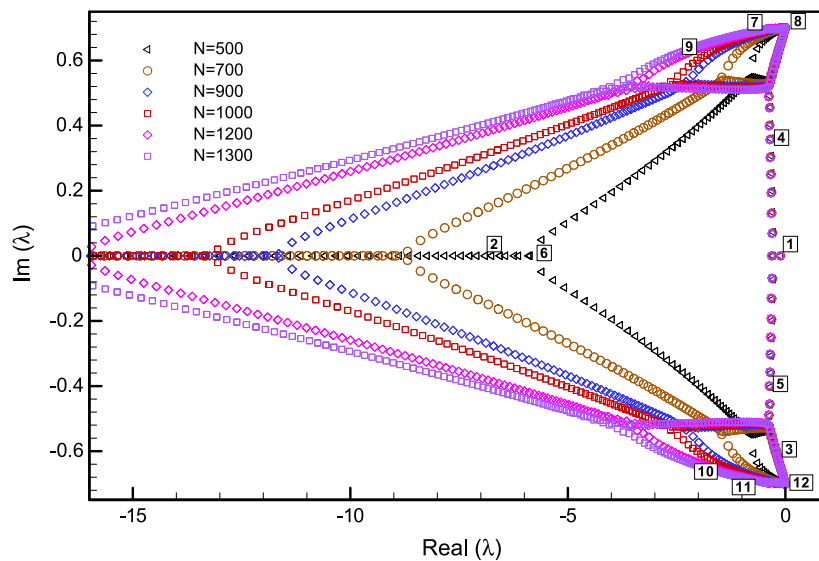


Figure 1. Spectrum of the mixing layer flow at $Re = 1000$, $\alpha = 0.7$ and $\beta = 1$ calculated for different numbers of grid points. Labeled points correspond to the eigenmodes shown in figure 2.

Table 3 shows an example of convergence of four leading eigenvalues belonging to the discrete part of the spectrum. It is seen that the use of 1000 grid points yields four converged decimal digits for the first mode; however the convergence slows down for the next modes. This shows that the linear stability analysis (Gelfgat and Kit 2006) is less computationally demanding than for the non-modal growth study, for which many leading eigenmodes must be calculated within a good accuracy.

Another way to verify the calculated growth function is to calculate the solution to (2) and (3) by integrating the ODEs with the optimal vector as the initial condition. In this case, the norm of the time-dependent solution at time t must be equal to the calculated growth function $G(t)$. In the following, the solution of the initial value problem is used for verification of the results, as well as to follow the time evolution of optimal vectors. For additional verification, we consider a fully non-linear time-dependent problem taking the optimal vector as an initial condition. The numerical technique used to solve the 3D problem is described in Vitoshkin and Gelfgat (2013). Comparison of the kinetic energy evolution with the growth function calculated via the three independent approaches is shown and discussed below.

4. The spectrum of a linearized problem

As with any flow in an unbounded domain, the mixing layer flow has two parts to the spectrum: a finite number of discrete eigenmodes and an infinite number of eigenmodes belonging to the continuous spectrum. Clearly, a numerical method, based on a discrete model defined for a bounded domain, cannot reproduce accurately the continuous modes. Grosh and Salven (1978) argued that continuous modes of the OS equation are either oscillatory or decaying functions located in free stream regions, where $U = \text{const}$ and $U' = 0$, and are zeroes in the regions where $U' \neq 0$. In our numerical results, we observe similar modes that slowly decay or oscillate towards the ends of the computational interval $[-L, L]$.

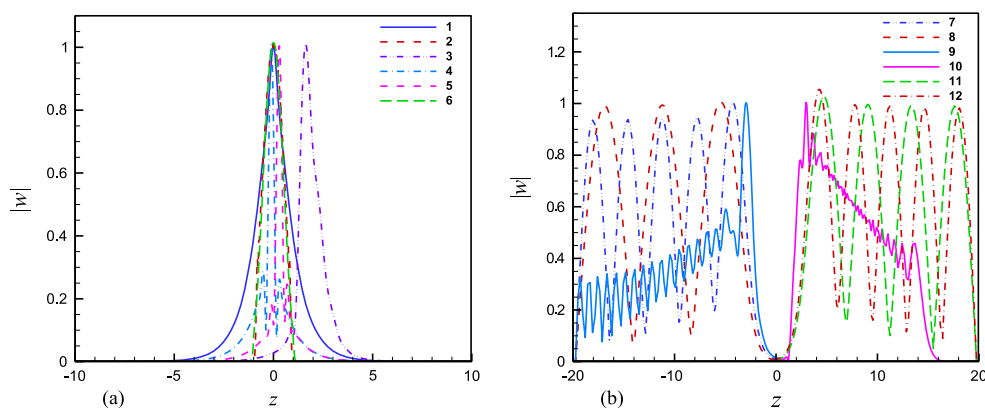


Figure 2. Patterns of eigenvectors belonging to (a) discrete and (b) continuous parts of the spectrum. $Re = 1000$, $\alpha = 0.7$, $\beta = 1$. The number of each line corresponds to the number of eigenvalues depicted in figure 1.

Their amount grows with mesh refinement; however, they are not exact zeroes in the shear zone (figures 1 and 2). The corresponding Gram matrix contains non-diagonal elements close to unity, which means that some modes are almost parallel with respect to the inner product (4). The latter can be expected for modes corresponding to the continuous spectrum of the unbounded problem. Furthermore, taking into account these almost parallel modes for computation of the growth function via the Gram matrix decomposition (Reddy and Henningson 1993) results in a very large growth function reaching values of the order of 10^{20} , with the corresponding optimal vector located inside the uniform flow. Apparently, such a result is considered to be unphysical and incorrect. Applying the calculus of variations, which is also based on the linearized problem spectrum, we arrive at a similar unphysical result. At this point, we assume that the observed almost parallel modes are a non-accurate replication of the continuous spectrum. Furthermore, we argue that the procedures described of Butler and Farrell (1992) and Reddy and Henningson (1993) are applicable only to a finite number of eigenmodes. Also, the continuous modes that do not decay far from the area of non-zero shear cannot be included in the analysis of growth in the norm (4), since the integral does not converge at $L \rightarrow \infty$, thus making all the procedures based on the chosen inner product meaningless, even if one assumes that a discrete approximation of the continuous spectrum is sufficiently accurate. Therefore, the effect of the non-decaying at $L \rightarrow \infty$ continuous spectrum on non-modal growth must be studied separately.

To account correctly for the problematic ‘continuous’ eigenmodes, we apply the third approach, which is based on the forward/backward time integration of the governing/adjoint equations, and therefore necessarily takes into account the entire spectrum (Corbett and Bottaro 2000). It can be seen (table 4) that all three approaches cross-verify each other and exhibit close results when applied to the Poiseuille flow, which is bounded and therefore has only a discrete spectrum. At the same time, when using the first two methods for the whole calculated spectrum of the mixing layer flow, we obtain a very large unphysical non-modal growth of the order of 10^{15} – 10^{20} . Note that the above observation disappears for the Blasius boundary layer flow, for which we leave all modes without separating them into discrete and continuous parts.

To apply the SVD approach, we extract the eigenvectors localized near the shear zone, as is illustrated in the following example. Consider a certain set of parameters $Re = 1000$, $\alpha = 0.7$

Table 4. The growth function, $G(t=5)$, calculated by different methods for Poiseuille flow, a boundary layer Blasius profile and mixing layer flow.

	Poiseuille flow $\alpha = 1, \beta = 0,$ $Re = 3000,$ (only discrete)	Blasius boundary layer $\alpha = 0.125,$ $\beta = 0.3, Re = 800,$ (discrete and continuous)	Mixing layer $\alpha = 1, \beta = 0,$ $Re = 1000,$ (extracted vectors)
Number of grid points, N			
using factorization of the Gram matrix—SVD			
500	5.44	1.77	14.66
1000	5.45	1.77	14.66
1500	5.45	1.77	14.66
applying the calculus of variations			
500	5.44	1.78	14.66
1000	5.45	1.77	14.66
1500	5.45	1.77	14.66
by iterative forward/backward integration of the governing/adjoint equations (the whole spectrum)			
500	5.44	1.76	14.66
1000	5.45	1.77	14.66
1500	5.45	1.77	14.66

and $\beta = 1$, for which we have non-modal growth. The calculated spectrum and examples of the eigenvector profiles are shown in figures 1 and 2. Three branches corresponding to the non-decaying continuous spectrum are given by $Imag(\lambda) = 0$ and the branches arriving at $Imag(\lambda) \approx \pm \alpha$ when $Real(\lambda) \approx 0$ (Grosch and Salwen 1978). As expected, these sets of eigenvalues do not converge and their number increases with the grid refinement, which is indicative of their ‘continuous’ origin. Conversely, the eigenmodes localized near the shear region can be recognized, primarily, by their fast convergence. Also, the number of these eigenmodes remains constant with the grid refinement, indicating that they originate from the discrete spectrum rather than the continuous one. For the following computations, we exclude eigenmodes whose amplitudes remain large for $|z| > 10$. We observe that the growth functions, as well as the number of extracted eigenvectors, do not change when boundaries of this interval vary from ± 8 to ± 15 , which shows that the procedure is consistent.

Following Mao and Sherwin (2012), we also performed the pseudospectrum analysis of the calculated spectrum. Figure 3(a) illustrates a calculated spectrum with the ε -pseudospectrum computed as the minimal singular value of the matrix $\mathbf{J} - \lambda \mathbf{I}$, where \mathbf{J} is the Jacobian matrix of the discretized equations system and λ is the current eigenvalue. We observe that the eigenmodes whose ε -pseudospectrum is relatively large, $\varepsilon > 10^{-4}$, do not decay in the free-stream region. The corresponding eigenvalues are characterized by $Imag(\lambda) \approx \pm \alpha$, which is also indicative of their ‘continuous’ origin, therefore those modes are excluded from calculations. At the same time, the eigenmodes whose ε -pseudospectrum is bounded by $\varepsilon > 10^{-5}$ coincide with the modes extracted according to the above arguments. An example of the growth functions calculated for only those modes whose pseudospectrum is bounded by either 10^{-5} , 10^{-6} or 10^{-7} , or is extracted as described above and corresponds to $\varepsilon > 10^{-4}$, is presented in figure 3(b). It is seen that modes corresponding to $10^{-5} < \varepsilon < 10^{-1}$ do not

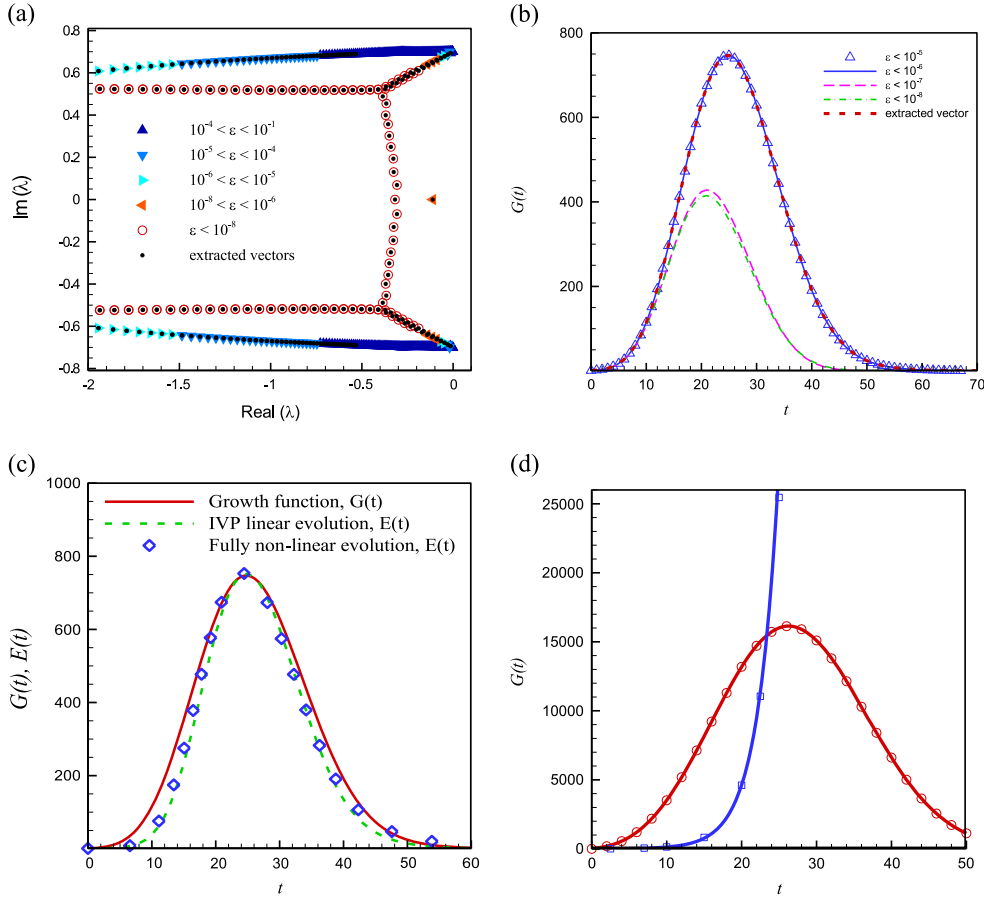


Figure 3. (a) The spectrum and pseudospectrum of the mixing layer flow at $\alpha=0.7$, $\beta=1$ and $Re=1000$. (b) Growth functions calculated for reduced parts of the spectrum corresponding to different values of the ϵ -pseudospectrum. (c) Comparison of the growth function $G_E(t)$ (solid line) with evolution of the kinetic energy of the optimal initial vector obtained as a solution of the ODEs IVP (dashed line) and as a solution of fully non-linear 3D problem (symbols). (d) Comparison of the growth function corresponding to a stable configuration at $\alpha=0.5$, $\beta=0.8$, $Re=1000$ (red line and circles) with the growth function calculated for the mean optimal growth rate reported by Arratia *et al* (2013) (blue line and squares).

contribute to the optimal growth, while the modes whose pseudospectrum $\epsilon < 10^{-6}$ do influence it. Therefore, we can conclude that the eigenmodes corresponding to $\epsilon < 10^{-6}$ are those to be accounted for. It is, however, emphasized that we still have no clear criteria to separate continuous and discrete parts of the spectrum.

The far right column of table 4 shows the results of the Gram matrix factorization/SVD approach of Reddy and Henningson (1993) and of the calculus of the variations method of Butler and Farrell (1992), both applied to the extracted eigenmodes only. It is clearly seen that these results are identical and are very close to those obtained by the iterative time-integration-based method, which accounts for the whole spectrum.

We also verified the behavior of the forward/backward time-integration-based method, starting the iterations from two different initial vectors. The initial profiles were chosen as a

wide parabola spreading into the uniform flow and with the Gaussian function located inside the mixing zone. In both cases, the same optimal vector was obtained after 5–6 iterations. We examined whether this observation remains valid for different values of Re , α and β , and concluded that even when the free stream area is artificially perturbed, the optimal vector remains located within the shear zone. Thus, we can restrict the non-modal analysis to only those eigenvectors that vanish outside the shear zone. It should be emphasized that having the spectrum computed, the Gram matrix factorization/SVD approach consumes significantly less CPU time than the one based on the forward/backward time integration, or than the computation of an inverse energetic matrix needed for the variational method. This is an advantage when, for example, optimal growth at different target times is studied.

For an additional verification of our conclusion, we used the calculated optimal vectors as the initial conditions for the ODE system (equations (2) and (3)), as well as fully 3D equation (1), and integrated them in time, monitoring the kinetic energy norm of the solution. We observed that at a chosen target time, the solution norm reaches the calculated value of the growth function. Clearly, if parts of to-be-continuous modes were perturbed inside the mixing zone and were contributing to non-modal growth, it would be impossible to obtain such a good agreement. In case a significant mode was mistakenly excluded, the real non-modal growth would be larger than the growth function calculated here. An example is shown in figure 3(c), where we compare the growth function calculated on the basis of the extracted discrete spectrum with the kinetic energy norm evolution yielded by time integration of the initial value ODEs and fully non-linear 3D problems. The equality of the maximal values of the norm and the growth function makes us confident in the results obtained, including the exclusion of the continuous spectrum.

Figure 3(d) compares the result of Arratia *et al* (2013) at $Re=1000$ with the growth function calculated for $\alpha=0.5$ and $\beta=0.8$. As mentioned above, these wavenumbers correspond to the largest non-modal growth we observe for a linearly stable configuration at $Re=1000$. The growth function of Arratia *et al* (2013) is calculated using the values of σ_{\max} reported in their figure 1(c) and their equation (3.6) as $G(t)=\exp(2\sigma_{\max}t)$. It should be stressed that in both studies, the optimal growth at small times, $t<10$, is found to be caused by a three-dimensional disturbances. However, as follows from figure 3(d), the non-modal growth found in the present work for $t<20$ is larger than that reported by Arratia *et al* (2013). Moreover, the optimal growth computed by Arratia *et al* (2013) for $10<t<20$ relates to linearly unstable configurations. As follows from our figure 3(d), in this time interval the non-modal growth still may exceed the exponential one. Clearly, the exponential growth exceeds the non-modal one at larger times.

5. Non-modal growth in the isothermal mixing layer flow

5.1. Growth function

The study of non-modal growth was started for two-dimensional disturbances ($\beta=0$), which, due to the Squire transformation, are mostly linearly unstable. Growth functions were calculated for $Re=100$, 1000 and 5000. Several examples are shown in figure 4. At large times, $t>10$, in all of the cases considered, the exponential growth of linearly unstable modes prevails over the non-modal growth. At short times, $t<10$, the non-modal growth of linearly stable modes with the streamwise wavenumber $\alpha\geq 0.9$ can slightly exceed the exponential growth of linearly unstable modes. As is shown below, this faster non-modal growth can lead to noticeable non-linear effects. An interesting observation is that among all *two-dimensional* modes exhibiting non-modal growth, the maximal one is attained by modes whose

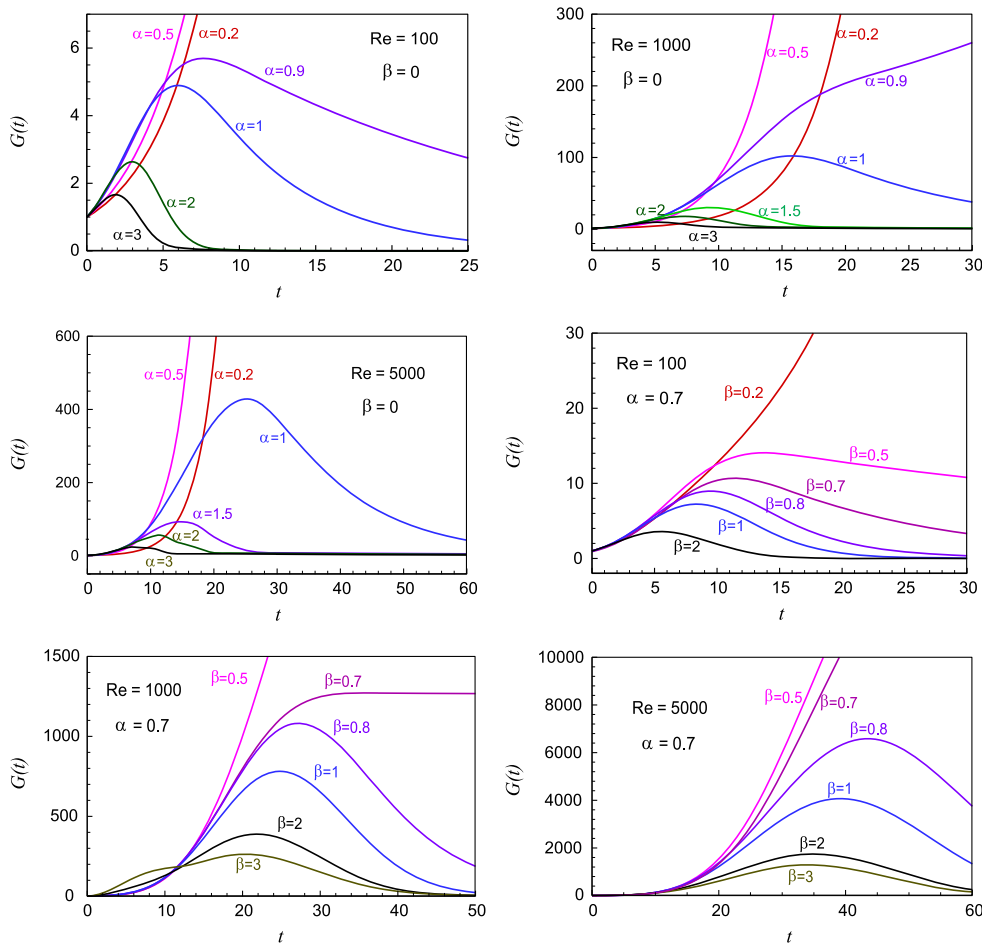


Figure 4. Growth functions of two-dimensional disturbances ($\beta = 0$) with $0.2 < \alpha < 3$ and three-dimensional disturbances ($\beta \neq 0$) for fixed $\alpha = 0.7$.

streamwise wavenumber α lays between values 0.9 and 1, i.e. the values that correspond to linearly stable modes in viscous ($0.9 < \alpha < 1$) and neutral modes in inviscid ($\alpha = 1$) mixing layers (Gelfgat and Kit 2006). It should be emphasized that non-linear numerical modeling and experimental studies are usually done at the values of α corresponding to linear instability, preferably with the largest time increment. The present results show that the non-linear evolution of stable and close-to-being-neutral modes is also worth exploring (see section 5.3).

Growth functions of three-dimensional disturbance modes at fixed values of the streamwise wavenumber $\alpha = 0.5, 0.7, 1$ and the varying spanwise wavenumber β are shown in figure 5. Note that the two-dimensional mode corresponding to $\beta = 0$ is linearly unstable in this case as well. The growth functions related to linearly unstable values of β are depicted by dashed lines, while we focus on the non-modal growth possible in linearly stable cases. As before, the calculations were performed for $Re = 100, 1000$ and 5000 . Also in these cases, we observe that for $Re \geq 100$ the non-modal growth can slightly exceed the linear one at short times, while at longer times, the linear exponential growth always prevails. We observe also

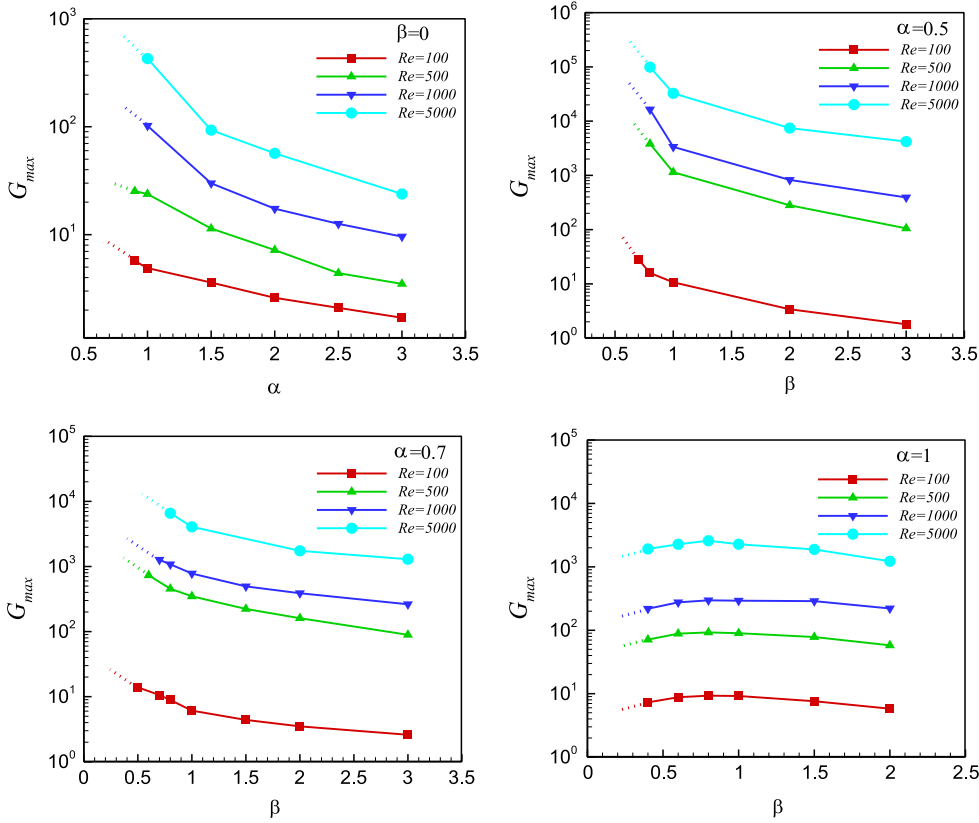


Figure 5. Values of G_{max} at $t=t_{max}$ for different α , β and Re (the dashed line depicts linearly unstable flow).

that the three-dimensional perturbations become stable when the spanwise wavenumber β exceeds a certain value close to 0.5. The most noticeable *three-dimensional* non-modal growth can be attributed to the values of β close to the linearly neutral configuration, when at least one eigenmode attains a small decay rate and slowly decays in time. This observation is maintained when we consider other fixed values of α and different values of β , as in figure 4. Table 5 summarizes the maximal values of the growth function, G_{max} , and the times at which the maximum is attained, t_{max} , over all wave numbers for 2D and 3D cases. The values of G_{max} at different α , β and Re are plotted in figure 5.

We observe here that the largest non-modal growth is three dimensional and is attained by oblique waves propagating at $(\alpha=0.5, \beta=0.8)$, with respect to the base flow. The well-known non-modal growth studies for Couette flow, Poiseuille flow (Butler and Farrell 1992, Reddy and Henningson 1993) and Blasius flow (Schmid 2000) also show that 3D perturbations exhibit the largest non-modal growth. This seems to be a common property of plane-parallel shear flows, which was discussed in detail in a recent paper by Vitoshkin *et al* (2012).

5.2. Optimal vector

For illustrative purposes, we chose characteristic parameters for 3D transient growth, namely $Re=1000$, $\alpha=0.7$ and $\beta=0.8$. At these parameters the flow is linearly stable, while non-

Table 5. Maximal values G_{max} and t_{max} and corresponding wave numbers.

$Re = 100$				$Re = 500$				$Re = 1000$				$Re = 5000$			
α	β	G_{max}	t_{max}	α	β	G_{max}	t_{max}	α	β	G_{max}	t_{max}	α	β	G_{max}	t_{max}
0.9	0	5.7	7.7	0.9	0	25.3	11.7	1.0	0	102.1	15.5	1.0	0	428.4	24.9
0.5	0.7	14.6	13.0	0.5	0.8	3.8e3	27.8	0.5	0.8	1.6e4	26.8	0.5	0.8	9.9e4	42.9

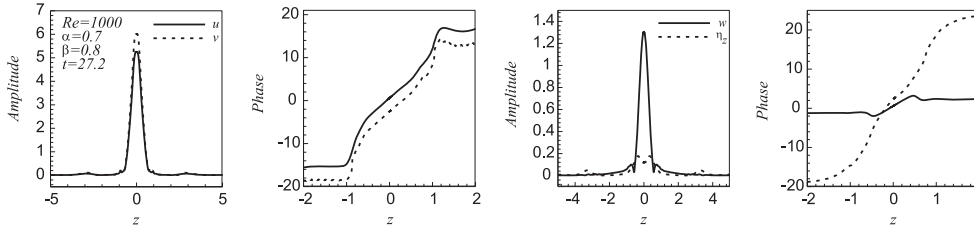


Figure 6. Amplitudes and phases of the optimal disturbance vector for $\alpha=0.7$, $\beta=0.8$ and $Re=1000$ for times yielding the maximal values of growth functions ($t_{max}=27.2$).

modal growth functions attain a maximal value that is close to the largest value over all possible spanwise wavenumbers. This choice allows us also to follow the time evolution of optimal vectors that will not be altered by an exponentially growing perturbation. Amplitudes and phases of the optimal vector are illustrated in figure 6. The optimal vectors are calculated for the target time $t_{max}=27.2$, at which corresponding growth functions attain their maximal values. For an additional verification of our results, we used the optimal vector as an initial condition for equations (2) and (3), and ensured that the time integration arrives to the final vector, as predicted by the first left singular vector of the corresponding SVD. The growth of amplitude yielded by the IVP solution also coincides with the predicted growth function value.

Comparing profiles of the optimal vectors with those of the leading eigenvectors (see, e.g., figure 3 in Gelfgat and Kit 2006) we observe that the optimal disturbance profiles are narrower and steeper. Contrarily to some of the eigenvectors, the optimal disturbance amplitudes are symmetric with respect to the mixing layer midplane.

5.3. Non-linear effect on evolution of the optimal vector

To gather a better insight into the time evolution of optimal disturbances, we also consider their fully non-linear development in time. It is emphasized that the following three-dimensional computations are aimed only to examine the development of optimal non-modal disturbances over long times, as it was done by Cherubini *et al* (2010) for boundary layer flow. Clearly, such results are irrelevant to a general problem of mixing layer flow, in which all possible disturbances are present.

Apparently, if the amplitude of optimal initial vector is small enough, the non-linear terms remain negligibly small during the whole time integration, so that the calculated flow resembles the predicted linear behavior. The growth of the initial perturbation kinetic energy coincides with one yielded by the IVP ODEs' solution, as well as with the growth function calculated by the SVD-based approach. This observation completes our verification of the non-modal growth results (see figure 3(c)).

To visualize the mixing layer flow, we follow Rogers and Moser (1992) and Kit *et al* (2010), and add a passively advected dimensionless temperature, T , to our model. Initially, the temperature is the same as the velocity \tanh profile. Figure 7(a) illustrates the kinetic energy growth of the optimal vector within the 2D mixing layer flow starting from an optimally perturbed base flow at parameters corresponding to the linearly stable case: $Re=1000$, $\alpha=1.5$ and $\beta=0$. The two cases presented in figure 7(a) correspond to two different amplitudes of the optimal disturbance vector. The optimal vector, whose kinetic energy norm is unity, appears to be small enough, compared to the base flow, and exhibits fully linear behavior over the whole time interval considered. It is shown by the solid line in figure 7(a).

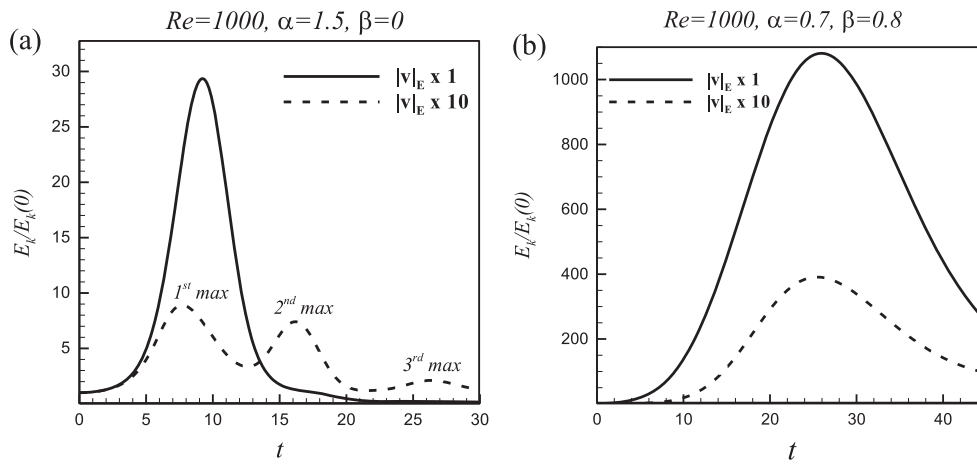
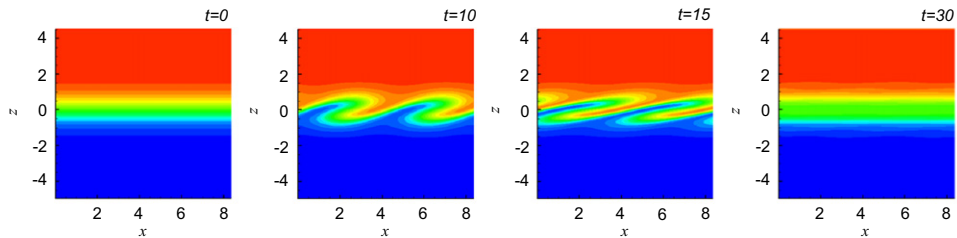


Figure 7. Kinetic energy growth of the optimal vectors with (dashed line) and without (solid line) the non-linear effect: (a) 2D and (b) 3D optimal disturbances.

(a) Linear evolution.



(b) Non-linear effect.

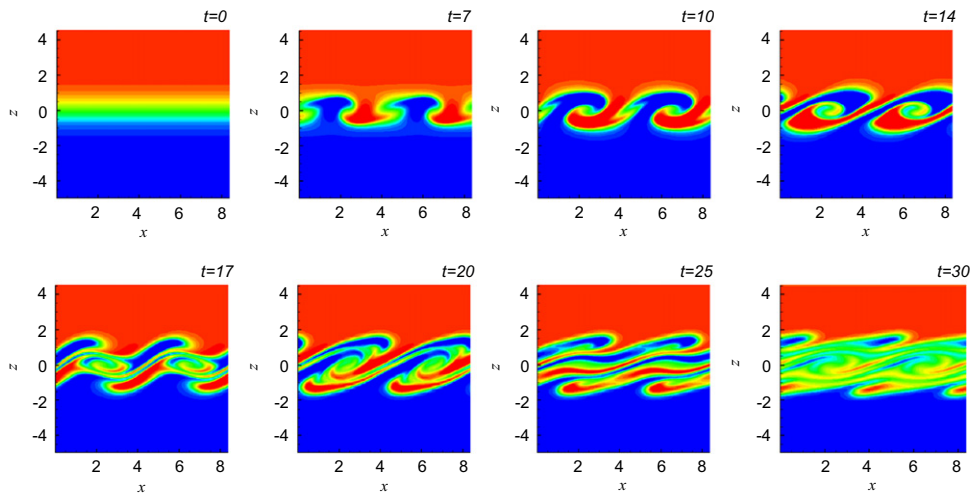


Figure 8. Snapshots of the passively advected temperature (heated flow above) in cases of the (a) linear and (b) non-linear time evolution of the optimal disturbance. $\alpha = 1.5$, $\beta = 0$, $Re = 1000$. The initial amplitude in case (b) is 10 times larger than that of case (a).

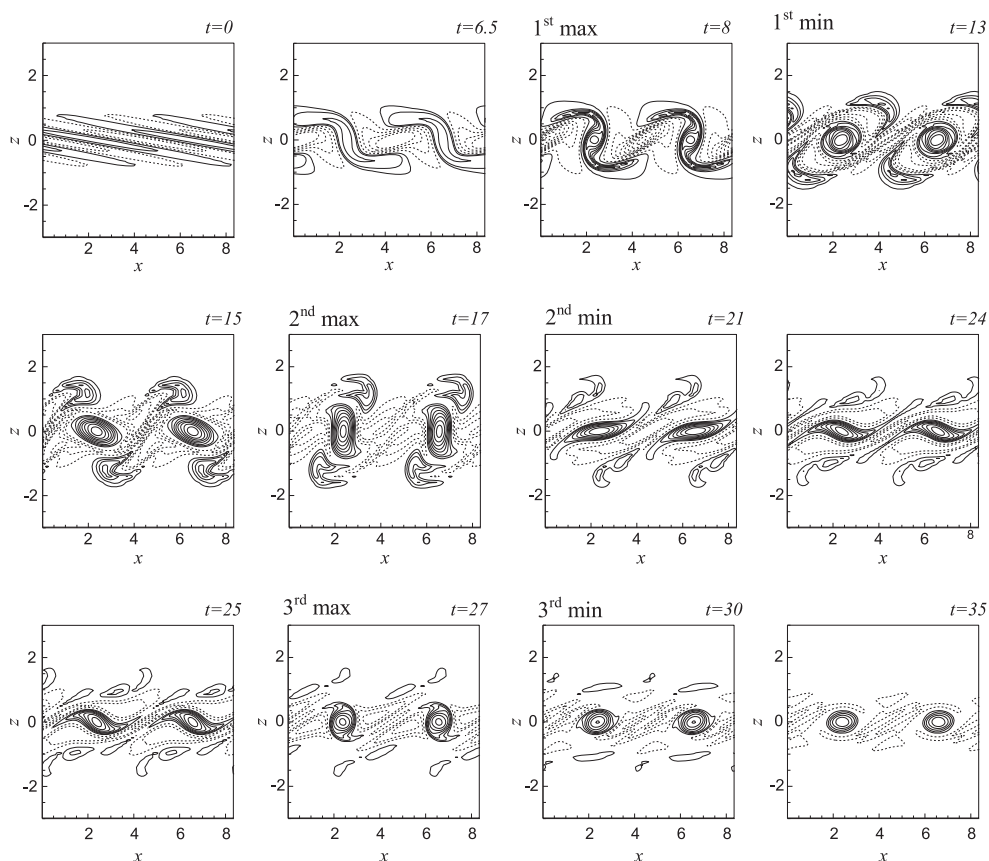


Figure 9. Snapshots of the spanwise vorticity during the non-linear time evolution of the optimal disturbance (solid and dashed lines indicate positive and negative contours, respectively) for $\alpha = 1.5$, $\beta = 0$ and $Re = 1000$.

Increasing the initial amplitude by a factor of 10 (dashed line in figure 7(a)), we observe linear behavior at the early times $t < 4$. At later times, the increased amplitude makes the non-linear terms non-negligible, which leads to a qualitatively different flow evolution that also includes a considerably smaller growth of kinetic energy, which, conversely to the linear predictions, attains several minima and maxima.

To illustrate the qualitatively different flow patterns, we compare the snapshots of the passively advected temperature T and the spanwise vorticity component in figure 8 and figure 9, respectively. The evolution of T in the fully linear case (figure 8(a)) exhibits zigzag wavy structures that disappear at longer times. The area where the passive scalar is completely mixed corresponds to the green color. An interesting observation is a wider zone of mixed T at large times compared to that in the initial state. A relatively fast mixing is achieved here together with the complete disappearance of the initial perturbation and laminarization of the perturbed flow.

When the evolution of the non-modal disturbance switches on the non-linear terms (figure 8(b)), one observes the appearance of the mushroom-shaped structures at $t = 7$ and 10. These structures look similar to the patterns of concentration reported in figures 13 and 14 of Lin and Corcos (1984) for a non-linearly developing mixing layer. Similar non-regular

structures were also observed in the streamwise plane experimentally by Bernal and Roshko (1986). At a later time, $t = 14$, the pattern becomes similar to the one reported by Smyth and Peltier (1991) in their figure 8. At a later time, $t = 17$, we observe the patterns with elongated borders, which resemble classical experimental observations of Thorpe (1971) at long times (see his figures 8 and 9). Obviously, after the optimal disturbance decays, the passive scalar appears to be mixed even more than in the previous case, while the flow attains the plane-parallel velocity profile.

Snapshots of the spanwise vorticity are shown in figure 9. At early times, the vorticity pattern consists of structures tilted against the main shear, whose optimal growth is based on the Orr mechanism (Orr 1907). At a later time we observe that vorticity patterns are rotated, apparently by the base flow, around their centers located at the midplane. Again, we see some similarities of the vorticity behavior with the fully non-linear results reported, e.g., by Rogers and Moser (1992) and Smyth and Peltier (1991).

It should be noted that we are examining the transient growth of optimal disturbance in order to discover the transition of a parametrically stable flow to an unstable regime. To do this, we increase the amplitude of the initial optimal perturbation so that non-linear terms will be triggered at later stages of the time evolution. The present calculations show that these non-linear effects do not lead to a noticeable subcritical transition. However, the optimal perturbation evaluates in a different way than that observed for a non-linear evolution of the most unstable linear eigenmode. As a calculation test, we performed non-linear computations using the KH mode as the initial vector and observed the well-known evolution of the spanwise vortices described, e.g., in Ho and Huerre (1984). As is seen from figure 9, the evolution of the optimal vector is governed mainly by the Orr mechanism and differs qualitatively from the evolution of the leading linearly unstable mode.

Comparing the vorticity perturbation pattern with the change of the growth function (cf figure 9 and figure 7(a)), we observe that when the kinetic energy norm reaches the minimum, the vorticity isolines are elongated along the shear slope. At later times they turn against the shear, which leads to the next temporal growth. The maximal values of the kinetic energy norm correspond to the vorticity patterns elongated vertically, exactly as was observed for the linearized problem.

Similarities between the computed flow structures and those observed in previous experimental and numerical studies allow us to make the following assumption. At late stages of time-development, the actual width of the mixing layer grows, thus leading to the growth of the dimensional streamwise wavenumber, α . This necessarily results in a stabilization of the mixing layer flow. However, at this stage the flow is already strongly perturbed. Therefore, it is possible that the development of the mixing layer flow at late stages is governed or strongly affected by the non-modal growth. The latter results in the flow structures similar to the ones observed here.

The time dependence of the kinetic energy norm for the 3D optimal disturbance is shown in figure 7(b). Similarly to the 2D case, the disturbance with the unity kinetic energy norm exhibits a completely linear behavior, and non-linear mechanisms switch on when the amplitude is increased by a factor of 10. However, in the 3D case the maximal growth of kinetic energy is attained at a considerably longer time (cf figure 4), as predicted by the above non-modal analysis. Note that in the 3D case, we do not observe several maxima and minima in the kinetic energy time history. Time evolution of the passively advected temperature is shown in figure 10. It generally resembles the structures observed in the 2D case; however the whole pattern is aligned along the disturbance vector $(2\pi/\alpha, 2\pi/\beta)$. After the perturbation decays, the width of the mixed temperature zone is even larger than that observed in the 2D case. The qualitative difference of the 2D and 3D non-modal growth can be seen by

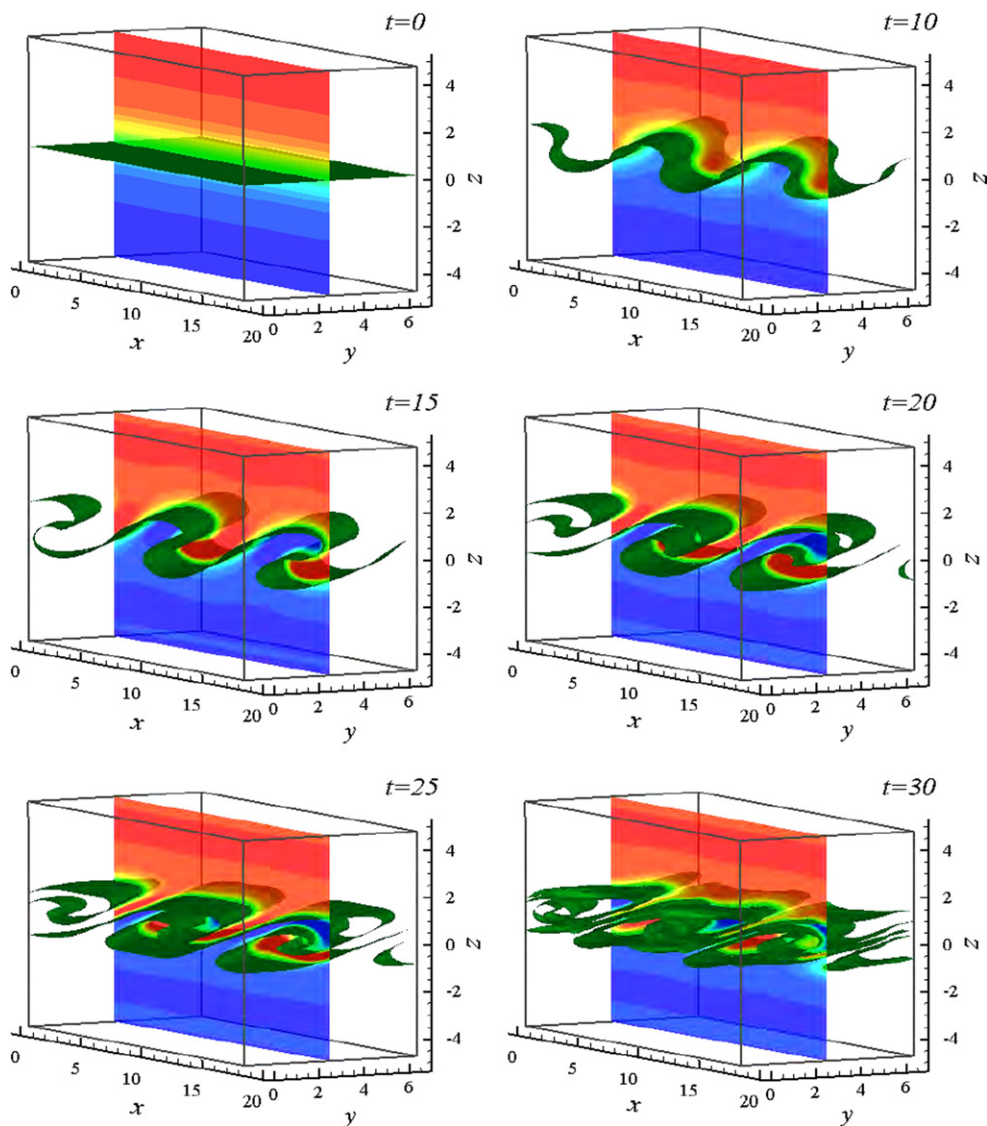


Figure 10. Snapshots of the passively advected temperature (heated flow above) during the non-linear time evolution of a 3D optimal disturbance, with $\alpha=0.7$, $\beta=0.8$ and $Re=1000$.

comparison of figures 9 and 11. Figure 11 shows the snapshots of spanwise vorticity in the spanwise midplane. Similarly to the 2D case, the 3D growth starts from the optimal perturbation aligned against the shear slope. However, when the perturbation becomes aligned along the shear ($t \geq 15$ in figure 11), the kinetic energy continues to grow, thus leading to a larger growth at a longer time. This phenomenon seems to be common for all plane parallel shear flows and has been addressed by Vitoshkin *et al* (2012).

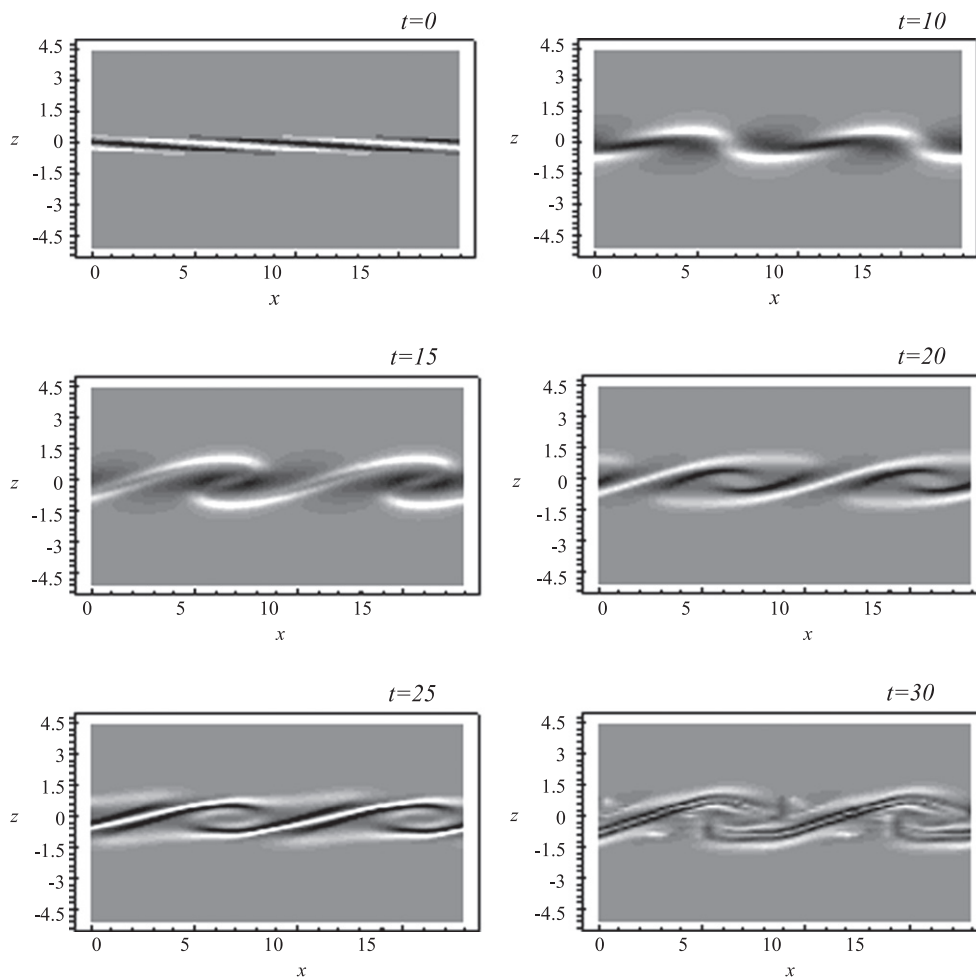


Figure 11. Snapshots of the spanwise vorticity in the spanwise midplane during the non-linear time evolution of the optimal disturbance, with $\alpha=0.7$, $\beta=0.8$ and $Re=1000$.

6. Conclusions

In the current study, transient perturbation dynamics in isothermal viscous mixing layers was investigated numerically. The convergence studies showed that an acceptable convergence can be reached by applying very fine and densely stretched grids with more than 1000 nodes in the cross-stream direction, which results in a large eigenvalue problem. To establish confidence in the obtained results on non-modal growth, the computations were performed using (i) the procedure offered by Reddy and Henningson (1993); (ii) the variational method offered by Butler and Farrell 1992; and (iii) the iterative forward/backward integration of governing/adjoint equations (Corbett and Bottaro 2000). Since the numerical model is bounded and its dimension is always finite, its spectrum is discrete. Analyzing the computed eigenvectors, we observed a part of them localized near the mixing zone, while the other part exhibits non-decaying oscillations toward the computational boundaries. The number of

localized eigenmodes remains constant independent of the grid refinement, which allows us to assume that they belong to the discrete part of the spectrum rather than to the continuous part. Approaches (i) and (ii) were applied for the localized part of the spectrum only, while approach (iii) included the entire spectrum. Since all three approaches yielded the same growth functions, we concluded that the non-localized part of the spectrum plays no role in the non-modal growth of the mixing layer flow. This conclusion was also supported by calculations of the ϵ -pseudospectrum (Trefethen and Embree 2005, Mao and Sherwin 2012), and was verified additionally by monitoring of the energy growth calculated via the ODEs' IVP problem, and the fully 3D time-dependent Navier–Stokes solution, both of which do not make any assumptions about the spectrum.

A series of numerical tests performed revealed that the mixing layer flow appears to be a more numerically challenging problem for non-modal growth analysis than for problems considering bounded (e.g., plane Couette and Poiseuille flows) or semi-inbounded (e.g., Blasius boundary layer profile) flows. The correct numerical modeling of the non-modal growth for the *tanh*-velocity profile requires much better resolution in the cross-flow direction than other plane-parallel flows.

The flow of interest exhibits significant transient growth, typically with streamwise and spanwise wavenumbers, for which the flow is asymptotically stable. It is emphasized that viscous mixing layer flow is linearly unstable starting from $Re_{cr} < 100$ (Gelfgat and Kit 2006), so that if all possible perturbations are present, the linear instability will prevail starting from rather early times. According to Arratia *et al* (2013) and the present results, a considerable non-modal growth can be observed at small times, even in the linearly unstable mixing layer flow. The large non-modal growth reported here can be observed if a perturbation with certain streamwise and spanwise periodicities is excited externally, like was done, e.g., in the experiments of Kit *et al* (2007). Arratia *et al* (2013) argued also that owing to the non-modal growth, linearly unstable modes can gain some additional energy at early times. This possibility was not explored in the present study.

Comparing the calculated flow structures with those observed in several previous experimental and numerical studies, we speculate that the mixing layer flow at late stages of the linear instability development can be strongly affected by the non-modal disturbances growth. The optimal perturbation is always localized inside the shear zone.

An issue that may need attention is the separation of the discrete and continuous parts of the spectrum. We offered several arguments on why and how the spatially localized part of the spectrum can be extracted and why only this part should be taken into account when the non-modal growth of disturbances in the isothermal mixing layer flow is studied. Since the number of spatially localized eigenmodes remained unchanged with the grid refinement, we assumed that all these eigenmodes belong to the discrete part of the spectrum. The corresponding results are verified by the three independent approaches for calculation of the growth function. An additional verification is supplied by the time-dependent calculations applied to the ODE system resulting from the discretized Orr–Sommerfeld and Squire equations, as well as to the fully 3D non-linear time-dependent flow model.

A three-dimensional direct numerical simulation of the mixing layer flow, which starts from the optimally perturbed base flow, was conducted to investigate the non-linear evolution of optimal perturbation and possibility for a by-pass transition. Following the time non-linear evolution of the optimal disturbances, we observe qualitatively different development in 2D and 3D cases. In the 2D case, the non-linear effects lead to the appearance of several maxima and minima in the kinetic energy time history. Evolution of the spanwise vorticity pattern reveals that the minima are observed when the iso-vorticity lines are tilted along the shear slope. The temporal growth starts when the isolines become tilted against the shear, and the

maxima are reached when they are rotated by the base flow until they become vertically aligned. No several minima or maxima are observed in the non-linear development of the 3D optimal disturbances. The maximum of the kinetic energy in the 3D case is attained significantly later, compared to the 2D case, after the patterns had turned in the base flow direction. It should be noted that Arratia *et al* (2013) reported a faster growth of linearly unstable modes owing to the non-modal mechanism. In the course of the fully nonlinear 3D modelling of this study, all the optimal perturbations decayed at sufficiently long times, and did not trigger linear instability with smaller wavenumbers, i.e., larger spatial periods, possibly because the computational domain was too short. At the same time, our results show a possibility of obtaining a significant mixing without making the flow turbulent. This observation is based on the advection of passive temperature and is observed during both 2D and 3D, linear and non-linear, evolution of an optimally disturbed mixing layer flow.

Acknowledgement

This study was supported by BSF (Bi-National US-Israeli Foundation) grant No. 2004087. The authors wish to express their thankfulness to E Kit and E Heifez for long and fruitful discussions of these results.

References

- Åkervik E, Ehrenstein U, Gallaire F and Henningson D S 2008 Global two-dimensional stability measures on the flat plate boundary-layer flow *Eur. J. Mech. B/Fluids* **27** 501–13
- Andersson P, Berggren M and Henningson D S 1999 Optimal disturbances and bypass transition in boundary layers *Phys. Fluids* **11** 134–50
- Arratia C, Caulfield C P and Chomaz J-M 2013 Transient perturbation growth in time-dependent mixing layers *J. Fluid Mech.* **717** 90–133
- Bakas N A and Ioannou P J 2009 Modal and nonmodal growths of inviscid planar perturbations in shear flows with a free surface *Phys. Fluids* **21** 024102
- Bernal L P and Roshko A 1986 Streamwise vortex structure in plane mixing layers *J. Fluid Mech.* **170** 499–525
- Bun Y and Criminale W O 1994 Early-period dynamics of an incompressible mixing layer *J. Fluid Mech.* **273** 21–82
- Butler R M and Farrell B F 1992 Three-dimensional optimal perturbations in viscous shear flows *Phys. Fluids A* **4** 1367–650
- Cherubini S, Robinet J-C, Bottaro A and De Palma P 2010 Optimal wave packets in a boundary layer and initial phases of a turbulent spot *J. Fluid Mech.* **656** 231–59
- Corbett P and Bottaro A 2000 Optimal perturbations for boundary layers subject to stream-wise pressure gradient *Phys. Fluids* **12** 120–30
- Criminale W O, Jackson T L and Lasseigne D 1995 Towards enhancing and delaying disturbances in free shear flows *J. Fluid Mech.* **294** 283–300
- Drazin P G and Reid W H 2001 *Introduction to Hydrodynamic Stability* (Cambridge: Cambridge University Press)
- Ellingsen T and Palm E 1975 Stability of linear flow *Phys. Fluids* **18** 487–8
- Farrell B F 1987 Developing disturbances in shear *J. Atmospheric Sc.* **44** 2191–9
- Farrell B F 1988 Optimal excitation of perturbations in viscous shear flow *Phys. Fluids* **31** 2093–102
- Gaster M, Kit E and Wynanski I 1985 Large-scale structures in a forced turbulent mixing layer *J. Fluid Mech.* **150** 23–39
- Gelfgat A Y and Kit E 2006 Spatial versus temporal instabilities in a parametrically forced stratified mixing layer *J. Fluid Mech.* **552** 189–227
- Grosch C E and Salwen H 1978 The continuous spectrum of the Orr-Sommerfeld equation Part 1. The spectrum and the eigenfunctions *J. Fluid Mech.* **87** 33–54

- Healey J J 2009 Destabilizing effects of confinement on homogeneous mixing layers *J. Fluid Mech.* **623** 241–71
- Heifetz E and Methven J 2005 Relating optimal growth to counterpropagating Rossby waves in shear instability *Phys. Fluids* **17** 064107
- Ho C-M and Huerre P 1984 Perturbed free shear layers *Ann. Rev. Fluid Mech.* **16** 365–424
- Kit E, Gerstenfeld D, Gelfgat A Y and Nikitin N V 2010 Bulging and bending of Kelvin-Helmholtz billows controlled by symmetry and phase of initial perturbation *J. Physics: Conference Series* **216** 012019
- Kit E, Wygnansky I, Friedman D, Krivonosova O and Zhilenko D 2007 On the periodically excited plane turbulent mixing layer, emanating from a jagged partition *J. Fluid Mech.* **589** 479–507
- Landahl M T 1980 A note on an algebraic instability of inviscid parallel shear flows *J. Fluid Mech.* **98** 243–51
- Le Dizès S 2003 Modal growth and non-modal growth in a stretched shear layer *Eur. J. Mech., B/Fluids* **22** 411–30
- Lin S J and Corcos G M 1984 The mixing layer: deterministic models of a turbulent flow. Part 3. The effect of plane strain on the dynamics of streamwise vortices *J. Fluid Mech.* **141** 139–78
- Mao X and Sherwin S J 2012 Transient growth associated with continuous spectra of the Batchelor vortex *J. Fluid Mech.* **697** 35–59
- Orr W M F 1907 The stability or instability of the steady motions of a perfect liquid and of a viscous liquid. Part II: A viscous liquid *Proc. Roy. Irish Acad.* **A27** 9–69
- Reddy S C and Henningson D S 1993 Energy growth in viscous channel flows *J. Fluid Mech.* **252** 209–38
- Rogers M M and Moser R D 1992 The three-dimensional evolution of a plane mixing layer: the Kelvin-Helmholtz rollup *J. Fluid Mech.* **243** 183–226
- Schmid P J 2000 Linear stability theory and bypass transition in shear flows *Physics of Plasmas* **7** 1788–94
- Schmid P J and Henningson D S 2001 *Stability And Transition In Shear Flows* (New York: Springer)
- Smyth W D and Peltier W R 1991 Instability and transition in finite-amplitude Kelvin-Helmholtz and Holmboe waves *J. Fluid Mech.* **228** 387–415
- Thorpe S A 1971 Experiments on the instability of stratified shear flows: miscible fluids *J. Fluid Mech.* **46** 299–319
- Trefethen L N and Embree M 2005 *Spectra and Pseudospectra: The Behavior of Nonnormal Matrices and Operators* (Princeton: Princeton University Press) p 624
- Vitoshkin H 2013 Computational modeling of two- and three-dimensional non-modal disturbances growth in homogeneous and stratified viscous mixing layer flows *PhD thesis* (Tel-Aviv University)
- Vitoshkin H and Gelfgat A Y 2013 On direct inverse of Stokes, Helmholtz and Laplacian operators in view of time-stepper-based Newton and Arnoldi solvers in incompressible CFD *Comm. Comput. Phys.* **14** 1103–19
- Vitoshkin H, Heifetz E, Gelfgat A Y and Harnik N 2012 On the role of vorticity stretching in optimal growth of three dimensional perturbations on plane parallel shear flows *J. Fluid Mech.* **707** 369–80
- Yecko P and Zaleski S 2005 Transient growth in two-phase mixing layers *J. Fluid Mech.* **528** 43–52
- Yecko P, Zaleski S and Fullana J-M 2002 Viscous modes in two-phase mixing layers *Phys. Fluids* **14** 4115–23